PCCP

Excited State Born-Oppenheimer Molecular Dynamics through a coupling between Time Dependent DFT and AMOEBA†

Michele Nottoli,[a] Benedetta Mennucci,[a] and Filippo Lipparini*[a]

We present the implementation of excited state Born-Oppenheimer molecular dynamics (BOMD) within a polarizable QM/MM approach based on a time-dependent Density Functional Theory (TDDFT) formulation and the AMOEBA force field. The implementation relies on an interface between Tinker and Gaussian software and it uses an algorithm for the calculation of QM/MM energy and forces which scales linearly with the number of MM atoms. The resulting code can perform TDDFT/AMOEBA BOMD simulations on real-life systems on standard computational resources. As a test case, the method is applied to the study of the mechanism of locally-excited to charge-transfer conversion in dimethylaminobenzonitrile in a polar solvent. Our simulations confirm that such a conversion is governed by the twisting of the dimethylamino group which is accompanied by an important reorentation of the solvent molecules.

1 Introduction

Excited state molecular dynamics is a powerful tool to study photoinduced processes, since it can be used to directly follow the system along its reaction path upon the initial excitation. For adiabatic processes, such simulations can be performed by computing, with an appropriate level of theory, the excited state energy and its derivatives with respect to the nuclear coordinates. The resulting forces can then be used to integrate the classical equations of motion, and the analysis of the trajectories can provide important insights on processes such as photochemical reactions, photoisomerizations, excited state intramolecular proton transfers and charge transfers.[1,2] The calculation of excitation energies is, however, an expensive task from a computational point of view. Assembling the gradients further aggravates the computational burden, which can easily become a formidable obstacle to performing molecular dynamics (MD) simulations. For these reasons, when dealing with large and complex systems, a fully quantum mechanical (QM) description is no longer feasible. This problem can be mitigated by employing a focused model, in which the region of interest is described with the QM method of choice, whereas the rest of the system is described with a much cheaper classical method, such as molecular mechanics (MM).[3–9]

Hybrid QM/MM schemes have been extended to molecular dynamics simulations, and successfully applied to many different systems and processes, both in the ground and in the excited states.[10,11] In standard QM/MM MD simulations, the coupling between the two subsystems is represented in terms of an electrostatic interactions between the set of MM point charges and the QM charge density which can thus be polarized. However, the classical subsystem is not able to polarize back in response to changes in the QM charge density. This limitation can become serious when photoinduced processes are investigated. A possible solution to this problem is the use of a polarizable MM description. There are many schemes available that implement MM polarization in different ways and that have been coupled to a QM description (see some recent reviews[10,12–14] and reference therein). Focusing on their extension to MD, a popular choice relies on induced point dipoles[3,12,15–24] (IPD), where polarization is achieved by endowing each classical atom with a polarizability.[24–27] Among IPD formulations, a very popular one is the AMOEBA force field,[28] for which QM/MM implementations have been developed.[29–31]

Including polarization effects in the classical description comes at a cost: polarizable QM/MM schemes are characterized by a higher computational cost than their non-polarizable counterparts. While this is already an issue in "static" QM/MM calculations, it can become a real barrier when the aim is to perform MD simulations. It is therefore of fundamental importance to achieve an implementation which is not only as highly optimized as possible, but also that presents a linear scaling in computational cost and memory requirements with respect to the number of MM atoms.[32,33]

In this contribution, we present the first implementation of an excited state Born-Oppenheimer molecular dynamics (BOMD) that couples TDDFT and the AMOEBA polarizable force-field.

[a] *Dipartimento di Chimica e Chimica Industriale, Università di Pisa, Via G. Moruzzi 13, 56124 Pisa, Italy*

∗ *E-mail: filippo.lipparini@unipi.it*

This is achieved through an interplay of Tinker[34,35] and Gaussian[36] softwares. This work builds up on the first implementation of excited state gradients with a polarizable MM embedding presented by one of the present authors[37] but it goes beyond it in two ways. First of all, it generalizes the gradients to AMOEBA force field and, more importantly, it is characterized by a computational cost which is linear in the size of the MM subsystem, thus allowing the method to be applied to large systems with a cost that is only slightly larger than that of the sole QM part. The Gaussian–Tinker interface, originally developed by Loco et al.[24,26], has been improved in efficiency and generalized to allow for excited state BOMD simulations.

This paper is organized as it follows. In section 2.1 we present the main theoretical aspects of the coupling between a TDDFT description and the AMOEBA force field going from the energy to the gradients. In section 2.2 we describe the modifications introduced in Tinker and Gaussian codes to achieve an efficient BOMD implementation. Finally, in section 3 we present an application to the characterization of the dimethylaminobenzonitrile excited state in acetonitrile.

2 Methods & implementation

2.1 Energy and gradients within a TDDFT/AMOEBA formulation

The total energy of a QM system embedded in an AMOEBA environment can be written as the sum of the purely QM energy, the bonded contributions from the MM part, and finally the Van der Waals and electrostatic/polarization contributions. These last three components account both for interactions within the AMOEBA environment and between AMOEBA and the QM part.

$$\mathscr{E}^{\text{QM/AMOEBA}} = \mathscr{E}^{\text{QM}} + \mathscr{E}^{\text{ele}} + \mathscr{E}^{\text{VdW}} + \mathscr{E}^{\text{Bond}} \quad (1)$$

Of all the terms we focus on the electrostatic/polarization component, since it plays a central role in both our embedding scheme and in our linear scaling implementation. In fact all the other terms are calculated within a purely classical framework using the potentials originally developed for the AMOEBA force field and the standard cut-off procedure implemented in Tinker.[34,35]

The electrostatic interactions are described through an accurate multipolar expansion whereas polarization effects are introduced through induced point dipoles. Each MM atom i bears a set of fixed partial charge q_i, point dipole $\boldsymbol{\mu}_i^s$ and point quadrupole $\boldsymbol{\Theta}_i$, as well as an isotropic polarizability α_i.[28] A peculiarity of AMOEBA is that the polarization energy is not variational in the induced dipoles. In fact, the energy is computed as the interaction of the induced dipoles with a MM electric field $\boldsymbol{E}_p$ which is different from the field $\boldsymbol{E}_d$ responsible for inducing the dipoles themselves. The two fields are computed according to two sets of exclusion rules for the neighboring atoms. The non variational nature of the energy poses a problem when deriving coupled QM/AMOEBA equations and needs to be considered carefully. This problem has already been addressed in other works, where a variational energy functional for the AMOEBA polarization has been introduced,[31,38] so we present directly the variational formulation of the energy, which requires two sets of dipoles induced

by the two different MM fields.

$$\mathbf{T}\boldsymbol{\mu}_d = \mathbf{E}_d + \mathbf{E}^{\text{QM}}$$

$$\mathbf{T}\boldsymbol{\mu}_p = \mathbf{E}_p + \mathbf{E}^{\text{QM}} \quad (2)$$

Here, $\boldsymbol{T}$ is the interaction matrix between the dipoles, $\boldsymbol{E}_p$ and $\boldsymbol{E}_d$ are the MM field computed according to the two different exclusion rules and $\boldsymbol{E}^{\text{QM}}$ is the field from the QM density. Each vector is the collection of the property at every MM site. The total energy can be written as the sum of the QM energy,

$$\mathscr{E}^{\text{ele}} = \mathscr{E}^{\text{MM}} + \boldsymbol{q}^\dagger \boldsymbol{V}^{\text{QM}} - \boldsymbol{\mu}_s^\dagger \boldsymbol{E}^{\text{QM}} + \boldsymbol{\Theta}^\dagger \boldsymbol{G}^{\text{QM}}$$

$$+ \frac{1}{2}\boldsymbol{\mu}_d^\dagger \mathbf{T}\boldsymbol{\mu}_p - \frac{1}{2}(\boldsymbol{\mu}_p^\dagger \mathbf{E}_d + \boldsymbol{\mu}_d^\dagger \mathbf{E}_p) - \frac{1}{2}(\boldsymbol{\mu}_p + \boldsymbol{\mu}_d)^\dagger \mathbf{E}^{\text{QM}}. \quad (3)$$

In eq. 3, the first term represents the electrostatic interaction of the fixed multipoles with themselves. The three following terms are the interaction of the fixed multipoles with the QM density, where $\boldsymbol{V}$, $\boldsymbol{E}$ and $\boldsymbol{G}$ are respectively electric potential, field and field gradient. Finally, the last three terms are the polarization energy, which includes the self interaction of the dipoles, i.e., the work needed to induce them, and their interaction with the fixed multipoles and QM density.

When a self-consistent field (SCF) scheme is used in combination with AMOEBA, the SCF and polarization equations 2 are solved self-consistently. At each iteration of the SCF method, we compute the two sets of induced dipoles (eq. 2), we assemble the embedding energy (eq. 3) and form the AMOEBA contribution to the SCF matrix (derivative of eq. 3 with respect to the density):[31]

$$\frac{\partial \mathscr{E}^{\text{ele}}}{\partial P_{\mu\nu}} = F_{\mu\nu}^{\text{ele}} = \boldsymbol{q}^\dagger \boldsymbol{V}_{\mu\nu} - \boldsymbol{\mu}_s^\dagger \boldsymbol{E}_{\mu\nu} + \boldsymbol{\Theta}^\dagger \boldsymbol{G}_{\mu\nu} - \frac{1}{2}(\boldsymbol{\mu}_p + \boldsymbol{\mu}_d)^\dagger \boldsymbol{E}_{\mu\nu} \quad (4)$$

where $P_{\mu\nu}$ is the μ, ν component of the SCF density matrix (here expressed on a atomic basis set). The coupling of the SCF problem to the equations for the induced dipoles (eq. 2) accounts for the mutual polarization between the QM and MM subsystems.

Once the SCF density and the induced dipoles are converged, it is possible to assemble the contributions to ground state gradients as the derivatives of eq. 3 with respect to the position of the atoms. Here it is convenient to split the case of QM atoms (∂_R) from that of MM atoms (∂_r), namely:[24,38]

$$\partial_R \mathscr{E}^{\text{ele}} = \boldsymbol{q}^\dagger \partial_R \boldsymbol{V}^{\text{QM}} - \boldsymbol{\mu}_s^\dagger \partial_R \boldsymbol{E}^{\text{QM}} + \boldsymbol{\Theta}^\dagger \partial_R \boldsymbol{G}^{\text{QM}} - \frac{1}{2}(\boldsymbol{\mu}_p + \boldsymbol{\mu}_d)^\dagger \partial_R \boldsymbol{E}^{\text{QM}}$$

$$\partial_r \mathscr{E}^{\text{ele}} = \partial_r \mathscr{E}^{\text{MM}} - \boldsymbol{q}^\dagger \boldsymbol{E}^{\text{QM}} + \boldsymbol{\mu}_s^\dagger \boldsymbol{G}^{\text{QM}} - \boldsymbol{\Theta}^\dagger \boldsymbol{H}^{\text{QM}} + \boldsymbol{F}_{\text{rot}}$$

$$+ \frac{1}{2}\boldsymbol{\mu}_d^\dagger (\partial_r \boldsymbol{T})\boldsymbol{\mu}_p - \frac{1}{2}\left(\boldsymbol{\mu}_p^\dagger \partial_r \boldsymbol{E}_d + \boldsymbol{\mu}_d^\dagger \partial_r \boldsymbol{E}_p\right) + \frac{1}{2}(\boldsymbol{\mu}_p + \boldsymbol{\mu}_d)^\dagger \boldsymbol{G}^{\text{QM}}$$
$$(5)$$

where $\boldsymbol{H}^{\text{QM}}$ is the electric field Hessian and $\boldsymbol{F}_{\text{rot}}$ is a term stemming from the matrices used to rotate the static multipoles from a reference frame to the lab frame.[39]

Excited state are here computed within a linear response formulation. Assuming now that the selected SCF method is DFT, excitation energies and transition densities are the eigenvalues

and eigenvectors of the Casida's matrix.[40] These are usually computed with an iterative scheme, such as the Davidson diagonalization.[41] Since the polarization component of the environment energy, $\mathscr{E}^{\text{ele}}$ is quadratic in the density (see eq. 3), it contributes to the linear response matrices with an explicit term:[31]

$$\frac{\partial^2 \mathscr{E}^{\text{ele}}}{P_{\mu\nu} P_{\kappa\lambda}} = \mathscr{V}^{\text{ele}}_{\mu\nu\kappa\lambda} = -\boldsymbol{E}^{\dagger}_{\mu\nu} \boldsymbol{T}^{-1} \boldsymbol{E}_{\kappa\lambda}. \quad (6)$$

From a physical point of view, this term models the electronic response of the environment to the excitation process and can be considered analogous to a non-equilibrium solvation contribution in continuum models[42], where only the electronic response of the solvent is considered to be instantaneous. At each iteration of the solver, given the transition density $\boldsymbol{P}^{\text{tr}}$, it is necessary to assemble its contraction with the term reported in eq. 6.

Gradients of the TDDFT energy, for a given electronic state, can be computed as derivatives of a time-dependent SCF Lagrangian $\mathscr{L}_i$, as proposed by Furche,[43] and later generalized to polarizable models.[37,44,45] Building the TD Lagrangian requires the $\boldsymbol{Z}$ and $\boldsymbol{W}$ Lagrange multipliers which are obtained by solving the Z-vector equations.[46,47] The reader is referred to the work of Menger et al.[37] for all the details of the extension of this method to a polarizable embedding formulated in terms of point dipoles. Here, we only report the contributions due to AMOEBA to the Lagrangian derivatives:

$$\partial \mathscr{L}^{\text{ele}} = \sum_{\mu\nu} P^{\Delta}_{\mu\nu} \partial F_{\mu\nu} + \sum_{\mu\nu\kappa\lambda} P^{\text{tr}}_{\mu\nu} P^{\text{tr}}_{\kappa\lambda} \partial \mathscr{V}^{\text{ele}}_{\mu\nu\kappa\lambda}. \quad (7)$$

The first term is the contraction of the relaxed difference density $\boldsymbol{P}^{\Delta}$ with the gradient of eq. 4, the second is the double contraction of the transition density $\boldsymbol{P}^{\text{tr}}$ with the gradient of eq. 6. The relaxed difference density depends on the eigenvectors of the Casida's matrix as well as on the $\boldsymbol{Z}$ vector.[43] Both the transition density and the relaxed difference density are specific of the chosen electronic state. An important aspect to note is that the first contraction is analogous to the one performed to assemble the gradients of the ground state, so it is convenient to assemble $\boldsymbol{P}^{\text{Tot}} = \boldsymbol{P}^{\text{SCF}} + \boldsymbol{P}^{\Delta}$ and compute both the ground state and excited state gradient contributions at the same time. For the second term, we separate the QM case from the MM one

$$\partial_R \mathscr{V}^{\text{ele}} = -2\boldsymbol{\mu}^{\dagger}_{\text{tr}} \partial_R \boldsymbol{E}_{\text{tr}}$$

$$\partial_r \mathscr{V}^{\text{ele}} = 2\boldsymbol{G}^{\dagger}_{\text{tr}} \boldsymbol{\mu}_{\text{tr}} + \boldsymbol{\mu}^{\dagger}_{\text{tr}} (\partial_r \boldsymbol{T}) \boldsymbol{\mu}_{\text{tr}} \quad (8)$$

with $\mathscr{V}^{\text{ele}} = \sum_{\mu\nu\kappa\lambda} P^{\text{tr}}_{\mu\nu} P^{\text{tr}}_{\kappa\lambda} \mathscr{V}^{\text{ele}}_{\mu\nu\kappa\lambda}$ and $\boldsymbol{T}\boldsymbol{\mu}_{\text{tr}} = \boldsymbol{E}_{\text{tr}}$. Here, there is a single set of induced dipoles since they do not depend upon the MM fields $\boldsymbol{E}_d$ and $\boldsymbol{E}_p$. The first expression contains the contraction of the induced dipoles with the derivative of the transition field, whereas the second expression contains the contraction of the induced dipoles with the transition field gradient and a term containing the derivative of the matrix.

To achieve an efficient implementation, it is necessary to keep the computational cost linear in the number of MM atoms, as this can easily become very large. To do so, the polarization equations have to be solved using iterative schemes, and the electro-

static properties from the MM atoms at the MM atoms have to be computed using efficient linear scaling algorithms.

The polarization equations have to be solved at each step of the SCF procedure, to find $\boldsymbol{\mu}_d$ and $\boldsymbol{\mu}_p$, and at each step of the Davidson method, due to the contraction of eq. 6 with the density is $-\boldsymbol{E}^{\dagger}_{\kappa\lambda} \boldsymbol{\mu}_{\text{tr}}$. For this reason it is crucial to use an efficient method. The most direct approach would be computing the inverse polarization matrix $\boldsymbol{T}^{-1}$ matrix and storing it in memory, however in this case the computational cost would scale as $\mathscr{O}(N^3_{\text{MM}})$ and the memory requirements as $\mathscr{O}(N^2_{\text{MM}})$, therefore the matrix inversion is a viable option only for small systems. A second option is to use an iterative solver that requires computing matrix–vector products $\boldsymbol{T}\boldsymbol{\mu}$ on the fly. This is the strategy that we pursue. In particular, we use a preconditioned conjugate gradient solver, using the preconditioner developed by Wang and Skeel.[48] For iterative solvers, the computational cost depends on the method used to compute the matrix–vector product. Note that the effect of the off-diagonal part of $\boldsymbol{T}$ applied to $\boldsymbol{\mu}$ results in computing the field of the dipoles at every other MM site, so in a straightforward implementation it scales as $\mathscr{O}(N^2_{\text{MM}})$. We overcome this bottleneck by computing the matrix-vector product using the fast multipole method (FMM)[49] as described in refs. 32 and 33.

The other computational bottlenecks from the environment contributions arise from the MM electrostatic at the MM atoms (which are $\mathscr{O}(N^2_{\text{MM}})$). Terms of this kind are the ones containing the derivative of the matrix $\partial \boldsymbol{T}$ in equations 5 and 7 and the ones appearing in the computation of the fixed multipole energy $\mathscr{E}^{\text{MM}}$ (eq. 3) and its gradient $\partial_r \mathscr{E}^{\text{MM}}$ (eq. 5). However, the same FMM machinery applied to the $\boldsymbol{T}\boldsymbol{\mu}$ product can be applied to these terms, as explained in ref 33.

2.2 TDDFT/AMOEBA Dynamics within a Gaussian-Tinker Interface

The implementation of the TDDFT/AMOEBA BOMD is here achieved interfacing a locally modified version of Gaussian 16,[36] and Tinker.[34,35]

Tinker drives the dynamics by performing the integration of the equations of motion, for which it requires the energy of the system and the forces. Those are assembled in different modules, each dealing with specific types of interactions; we use the original Tinker modules for the bonded and dispersion–repulsion interactions, whereas for the electrostatics and for the QM subsystem we use a custom module. This module sets up the input files for the QM calculation, calls Gaussian and then reads back the forces and properties. With respect to the previous implementation of the Tinker-Gaussian interface developed by some of us for ground state BOMD,[24,26] now the communication between the two softwares is performed via binary files to achieve better performance. A schematic representation of the interface is reported in fig. 1.

A user-provided list of QM atoms indicates which interactions (bonded, dispersion–repulsion, electrostatics) are to be computed by Tinker and which region is handled by Gaussian.

As it regards bonded interactions, two different cases are possible. If there are not covalent bonds between the QM and MM
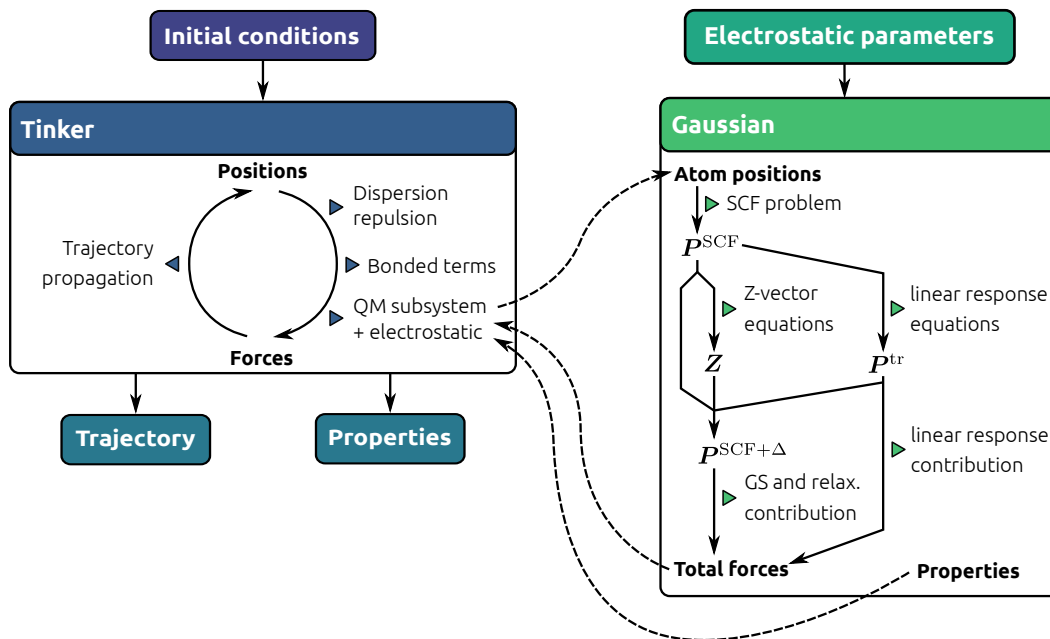
Fig. 1 Scheme of the Tinker–Gaussian implementation of the excited state BOMD. The dashed arrows represent communication between the two programs performed through binary files.

subsystems, QM atoms are simply excluded and only interactions between MM atoms are considered, which is easily achieved by just skipping atoms in the QM list. If bonds are present between QM and MM atoms, a pseudobond scheme, as implemented in previous works,[26,50] can be applied or, alternatively, a newly implemented link-atom scheme can be used.[7] Here we describe the implementation of the link-atom scheme only.

Within this framework, specific bonded terms have to be included at the interface between the QM and MM parts. Using the connectivity for guidance, we exclude all the interactions that involve bonds between two or more QM atoms, as these are already included in the QM energy. This is easily achieved by counting, for each bonded energy term, how many QM atoms are involved. More specifically, bonded terms are included if between MM atoms (no QM atom in the pair) or between a MM atom and the linked QM atom (one QM atom in the pair) and excluded otherwise (two QM atoms in the pair). Following the same logic, we include bendings if no more than one QM atom is involved, that is, if the interaction involves either three MM atoms or two MM atoms and the linked QM atom, and exclude them otherwise. As for torsional energy terms, that are defined by four atoms, we include them if no more than two of such atoms belong to the QM region, i.e., only if the torsion is around a MM bond or the bond connecting the QM and MM regions. A schematic representation of the included bonded terms is provided in fig. 2.

The AMOEBA force field includes other interactions such as out-of-plane bending and improper torsions, that are used to improve the description of partially double bonds and other complex chemical topologies. We include out-of-plane bendings only if the linked QM atom is just used as a reference to define the interaction and not if it is the atom undergoing pyramidalization, as we believe that if such an interaction is important, it should be
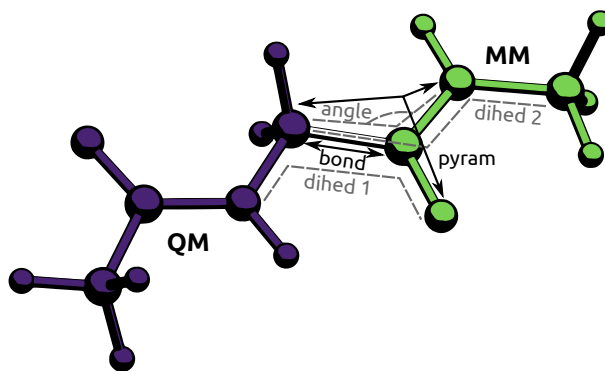

Fig. 2 Schematic representation of the bonded interactions at the QM–MM interface. All the possible cases are drawn: pyramidalization with a QM atom used as reference point, angle, bond, and two dihedrals comprising one and two QM atoms.

included in the QM subsystem. Analogously, no other advanced interactions are allowed at the boundary in our implementation.

Moving to dispersion–repulsion interactions, as they are to be computed not only between MM atoms, but also between QM and MM atoms, we exclude this type of interaction only when the two involved atoms belong to the QM subsystem; in this case in fact the interactions are already accounted for at the QM level. Finally, no electrostatic nor polarization interactions are computed by Tinker.

The electrostatic and polarization energy and forces are computed in the interface module, that handles the communication between the Tinker and Gaussian codes and runs the QM calculation. First, it creates the required input files for the Gaussian calculation, launches the calculations and finally reads the final energy which includes the QM component and all the electrostatic and polarization contributions, and the corresponding

forces (and other properties of the QM subsystem if requested). When a TDDFT dynamics is performed, the energy will correspond to the sum of the SCF energy and the excitation energy to the selected state.

As already reported, for QM and MM regions connected through covalent bonds, we implemented the link atom scheme in a way that it is entirely handled by Tinker. The interface module has to add a capping hydrogen for each broken QM/MM bond, such that the QM part is saturated. When the forces are read from Gaussian, the ones acting on these additional hydrogens have to be projected to the real atoms of the system.[7] Let r_{QM} and R_{MM} be the positions of the two atoms that define the bond that needs to be cut. The capping hydrogen atom is placed at

$$r_H = r_{QM} + k\hat{d}_{MM\text{–}QM}, \qquad (9)$$

where $\hat{d}_{MM\text{–}QM}$ is a short notation for $\frac{R_{MM} - r_{QM}}{|R_{MM} - r_{QM}|}$ and the parameter k is a constant set *a priori,* which defines the distance between the capping hydrogen and the QM atom. The QM software computes a force on the capping hydrogen, which can be projected on the two physical atoms by simply applying a chain rule. The corresponding equations can be found in section 1 of the ESI. Some MM interactions at the interface between the QM and MM parts have to be included as well: these forces are accounted for in the bonded modules by implementing the rules described previously. To avoid artificial effects, the QM–MM electrostatic interactions are removed for all the MM atoms that are within 2 or 3 bonds (as specified by the user) from the QM atom(s) connected to the added hydrogen(s). The total removed charge is then redistributed on the neighboring heavy MM atoms, in order to recover neutrality.

We conclude this section by noting that the interface here developed to perform QM/MM molecular dynamics also allows one to perform geometry optimizations, using Tinker as the main driver.

3 A test case: the LE-ICT conversion of DMABN in acetonitrile solution

Dimethylaminobenzonitrile (DMABN) is a well-known molecule that exhibits a dual fluorescence phenomenon which strongly depends on the solvent. More in details, the initial excitation populates the S2 state but within a few tens of femtoseconds the system undergoes internal conversion into to the lowest excited state (S1). Soon after, DMABN shows a (normal) fluorescence band which, in solvent of sufficiently high polarity, rapidly (on a scale of ps) decreases in intensity while a red-shifted second band starts to appear. The intensity ratio of the two bands finally stabilizes to a value which strongly depends on solvent polarity. It is now widely accepted that the normal fluorescence arises from a locally excited state (LE), whereas the red-shifted fluorescence arises from an intramolecular charge-transfer state (ICT).[1]

The LE–ICT conversion has been largely studied by time resolved spectroscopy and computational approaches.[51–62] However, the main geometrical changes involved in such a conversion have not been fully clarified and different mechanisms have been proposed (for a detailed review see the recent article by Kochman
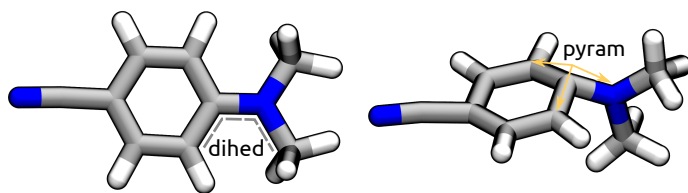

Fig. 3 DMABN structure showing the two coordinates mostly coupled with the excitation energy. Left: dihedral between the dimethylamino moiety and the phenyl ring. Right: pyramidalization at the aromatic carbon.

and Durbeej[62]).

The goal here is the characterization of the geometrical and electronic changes involved in the adiabatic conversion between LE and ICT. As such, we limit the dynamical description to the S1 state and completely neglect the ultrafast S2–S1 internal conversion. On the other hand, in the present analysis, the effect of a polar solvent (acetonitrile ACN) is taken into explicit account through the AMOEBA force field.

3.1 Computational details

Initial conditions for the excited state BOMD simulations were generated by a two step process.

First, we sampled the degrees of freedom of the solvent using a classical molecular dynamics trajectory using the GPU implementation of the Amber 18 package.[63] The initial configuration was built by placing DMABN at its optimized structure in a box made of 5524 acetonitrile (ACN) molecules, using the tleap module of the Amber suite. We used the generalized Amber force field (GAFF)[64] for both DMABN and ACN. The system was equilibrated by 50 ps of NVT dynamics and 1000 ps of NPT dynamics; the equilibrated box side measured 76 Å. Then, the equilibrated system was used to perform 60 ns of classical MD in the NPT ensemble with a temperature of 300 K. The temperature was controlled using Berendsen thermostat,[65] and the pressure was controlled using Monte Carlo barostat.[66] In all the steps the DMABN structure was kept frozen using harmonic restraints and we used a time step of 2 fs in combination with the SHAKE algorithm,[67] we used a cut-off of 12 Å for non bonded interactions, and the particle mesh Ewald method for long range electrostatic.[68]

In the second step, we extracted 16 frames from the last 10 ns of the MM trajectory to be used as a starting point for the DFT/AMOEBA BOMD simulations. For each frame, we kept the DMABN molecule and all the solvent molecules within 25 Å to define the initial configurations. A further equilibration step was performed for all the extracted configurations by performing 3 ps of DFT/AMOEBA NVT dynamics at 300 K, where the CAM-B3LYP functional with the 6-31+G(d) basis set was used to describe the DMABN molecule. Classical parameters for acetonitrile and dispersion–repulsion parameters for DMABN were taken from the AMOEBA09 force field included in the Tinker package.[69–71]

After such preliminary equilibration, we performed 2 ps of NVE adiabatic dynamics in the first excited state using the velocities and positions of the GS dynamics as starting conditions. The DMABN molecule was described using TDDFT at the same
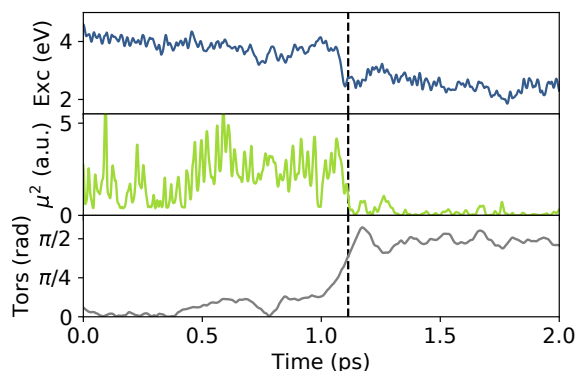
Fig. 4 Properties along an excited state trajectory. The jump in the state character is highlighted with a vertical dashed line.
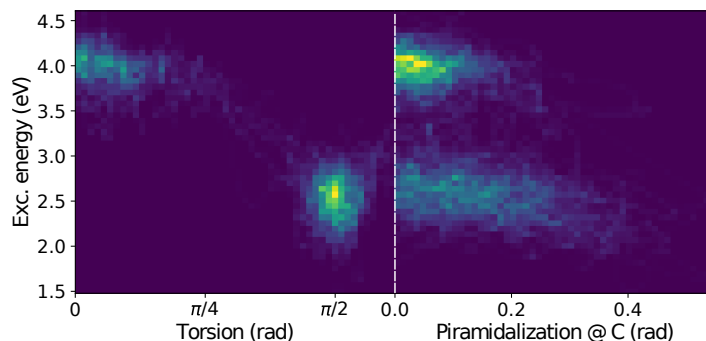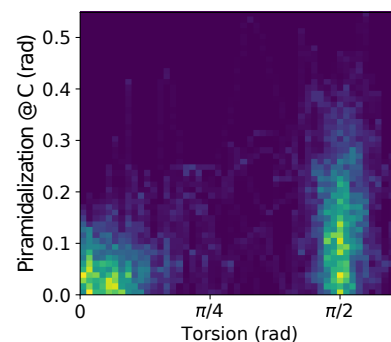

Fig. 5 Top: 2d histogram of the two investigated coordinates; bottom left: 2d histogram of the excitation energy and the torsion angle, bottom right: 2d histogram of the excitation energy and the pyramidalization angle.

level of theory used for the ground state equilibration. For the QM/AMOEBA simulations we employed a time step of 0.5 fs and we did not enforce boundary conditions, however we included a large amount of MM molecules to preserve the density of the inner region, where the DMABN molecule resides. Considered the short length of the trajectories, the strategy was successful: further proof is given in section 2 of the ESI. We remark, however, that longer simulations and/or simulations including fewer solvent molecules require boundary conditions, such as a frozen layer of solvent molecules or a restraining potential.[72,73] Analysis of the dynamics was performed using the python bindings to the CPPTRAJ tool.[74,75]

3.2 Results and discussion

Since the time evolution of the 16 trajectories is similar, we analyze here a single trajectory: the others are reported in section 3 of the ESI. As shown in the Fig. 4, at around 1.1 ps the excitation energy and the transition dipole moment suddenly drop whereas the dimethylamino–phenyl (DMA–Phe) dihedral angle changes from an almost planar to a twisted conformation. The same geometrical change is consistently observed in each of the 16 trajectory suggesting a twisted ICT state.

To have a more detailed analysis of the geometrical distortions involved in the LE–ICT conversion, we searched for correlations between some relevant coordinates and the excitation energy. Two coordinates turned out to be relevant: the expected DMA–Phe torsion and the pyramidalization at the aromatic carbon connected to the DMA group (see Fig. 3). The latter coordinate was already suggested by previous CC2 calculations as an important one for the evolution of the excited state.[54] The investigated correlations are reported in figure 5 as scatterd plots. The correlation plots between the excitation energy and the two selected coordinates shows that the main drop (∼1.5 eV) comes from the DMA–Phe torsion, but the pyramidalization contributes with an additional red-shift of up to 0.5 eV. Moreover, from the correlation between the two coordinates we can see that the pyramidalization is unlocked only in the twisted conformation.

The second aspect we addressed is how the changes in the electronic density and geometry of the DMABN excited state affect the solvent. To do this we first analyzed the electrostatic properties of

DMABN and then we investigated the solvent distribution along the dynamics.

A visualization of the changes in DMABN electronic density was obtained by performing three single point calculations, one for the ground state, and two for the S1 state at two geometries extracted from the S1 trajectories. The latter are defined by taking the subsets of the 16 trajectories before and after the drop in excitation energy, respectively, thus splitting them into a S1–LE and a S1–ICT trajectories. The geometries where then extracted from the corresponding trajectories. The electrostatic potential for the three cases is shown in figure 6. As expected, from the plots it clearly appears that the dipolar character of DMABN becomes more and more pronounced going from the ground to the LE state, and finally to the ICT state. The latter shows a clearly positive potential on the DMA residue confirming the charge-transfer character. The magnitude of the dipole moment for the ground and two excited state structures are 8.7, 13.2 and 19.6 Debye, respectively.

In order to gain a detailed insight into the configuration of the ACN molecules in the first solvation shells around DMABN and its change along the S1 evolution, we computed both radial distribution functions (RDF) and volume distributions for DMABN in the ground, S1–LE and S1–ICT states. For the ground state analysis we used the last part of the GS equilibration, whereas for the excited state analysis we used the splitted S1–LE and S1–ICT trajectories, as defined before.

The RDFs computed on the GS are plotted in fig. 7 whereas those computed on the S1–LE and S1–ICT are plotted in fig. 8. We computed the distribution of the ACN nitrogen and ACN
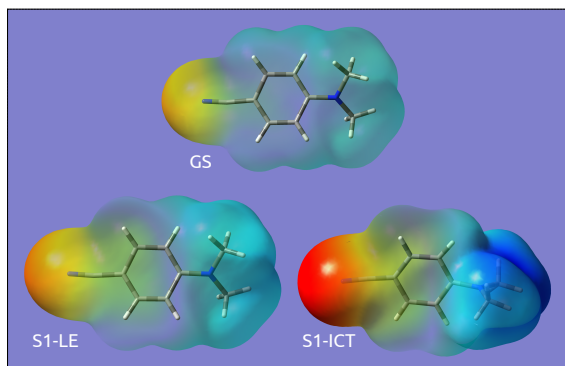
Fig. 6 Visualization of the electrostatic potential mapped on a density isosurface for ground (GS) and two excited state structures (S1-LE and S1-CT). The two S1 structures have been extracted at the beginning and at the end of a S1-BOMD trajectory. The same arbitrary scale has been used for the three plots: red refers to negative values, blue to positive values.
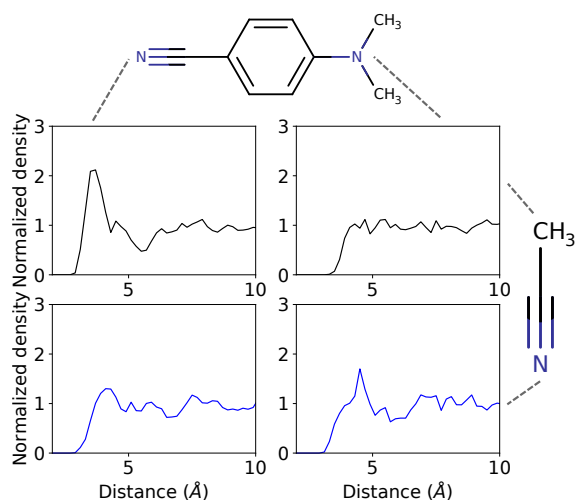

Fig. 7 Radial distribution functions computed on the GS dynamics. The four plots refer to different combinations of ACN methyl groups and ACN nitrogen combined with DMABN amino nitrogen and DMABN nitrile nitrogen — the correspondence is shown with the two molecular structures.
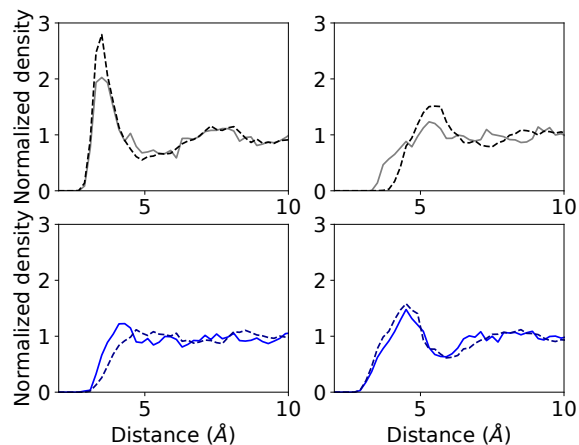

Fig. 8 Radial distribution functions computed on the S1–LE state (solid line) and on the S1–ICT state (dashed line). The four plots refer to different pairs of atoms used to compute the radial distribution functions as detailed in fig. 7 caption.

similar (bottom right panel) indicating that the solvent molecules rapidly rearrange according to the rotated DMABN (see also the twisted lobes in fig. 9).

In conclusion, the results of the TDDFT/AMOEBA BOMD confirm the twisting as the main geometrical distorsion leading to the ICT state and they show the importance of the rapid reorientation of the solvent molecules to stabilize the TICT structure.

methyl groups at the DMABN nitrile nitrogen and DMA nitrogen, for a total of four RDFs. the volume distribution of the solvent around DMABN nitrile and DMA nitrogens for the three investigated states are instead shown in Fig. 9.

The RDFs and volume distributions suggest a very similar solvent coordination in the ground and S1–LE states: this was expected due to both the similar dipolar and structural properties of the two states and the very short permanence of the S1–LE state before the twisting. As expected from the dipolar character of DMABN, we observe a preferential distribution of ACN molecules with the methyl groups pointing towards the DMABN nitrile (but without a well defined direction) and with the nitrile group coordinating the DMABN amino nitrogen from above and below its molecular plane as confirmed by the two lobes in the solvent volume density (see 9). Moving from the S1–LE to the S1–ICT state, the nitrile–methyl RDF (top left panel in Fig. 8) becomes sharper, whereas the DMA–nitrile coordination remains
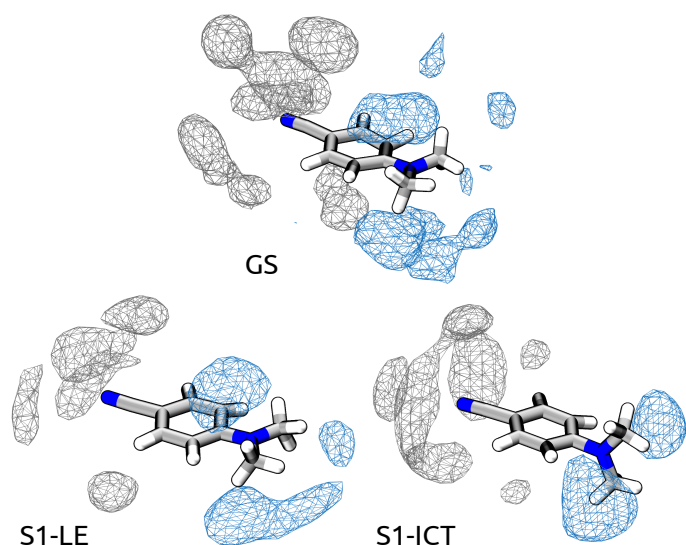
Fig. 9 Visualizations of the solvent distribution around DMABN. Blue: distribution of ACN nitrogen within 4.5 Å of DMABN amino nitrogen. Black: distribution of ACN methyl groups within 4.5 Å of DMABN nitrile nitrogen.

4   Summary

In this paper, we have presented the implementation of TDDFT/MM molecular dynamics within a polarizable embedding based on the AMOEBA force field.

The implementation relies on the interface between Tinker and Gaussian softwares. The former propagates the trajectory and computes forces and energies arising from classical dispersion-repulsion and bonded interactions. Forces and energies arising from the QM subsystem and from all the electrostatic and polarization interactions are instead calculated by Gaussian. The main aspects of novelty of the present implementation can be summarized as follows:

- The extension, for the first time, of the linear scaling machinery presented in ref. 33 to excited states molecular dynamics. This means that all computations, including the purely MM terms, the mutually polarized SCF contributions, the response and Z-vector contributions and the explicit force contributions are computed at a cost that scales linearly with respect to the number of MM atoms.

- A completely rewritten, efficient implementation of the polarizable QM/MM contributions to the TDDFT gradients.

- An improved Gaussian-Tinker interface that, besides using an optimized I/O protocol, can also treat covalent bonds between the QM and MM regions using link atoms.

A test application on the LE–ICT conversion of DMABN in acetonitrile solution confirms the potential of such an approach in investigating molecular systems for which the environment plays a fundamental role in determining their exited state properties and dynamics.

All the TDDFT/AMOEBA BOMD simulations described in this communication were performed on a single computer node, which demonstrates that the methodology is accessible even when only moderate computational resources are available, paving the way for new extensions and applications.

Acknowledgments

Notes and references

1 Z. R. Grabowski, K. Rotkiewicz and W. Rettig, *Chem. Rev.*, 2003, **103**, 3899–4032.

2 T. Kumpulainen, B. Lang, A. Rosspeintner and E. Vauthey, *Chem. Rev.*, 2016, **117**, 10826–10939.

3 A. Warshel and M. Levitt, *J. Mol. Biol.*, 1976, **103**, 227–249.

4 Johan Åqvist and Arieh Warshel, *Chem. Rev.*, 1993, **93**, 2523–2544.

5 A. Warshel, *Annu. Rev. Biophys. Biomol. Struct.*, 2003, **32**, 425–443.

6 H. Lin and D. G. Truhlar, *Theor. Chem. Acc.*, 2006, **117**, 185–199.

7 H. M. Senn and W. Thiel, *Angew. Chem. Int. Ed.*, 2009, **48**, 1198–1229.

8 Stefan Dapprich and István Komáromi and K.Suzie Byun and Keiji Morokuma and Michael J Frisch, *J. Mol. Struct.: Theochem*, 1999, **461-462**, 1–21.

9 Thom Vreven and K. Suzie Byun and István Komáromi and Stefan Dapprich and John A. Montgomery and Keiji Morokuma and Michael J. Frisch, *J. Chem. Theory Comput.*, 2006, **2**, 815–826.

10 E. Brunk and U. Rothlisberger, *Chem. Rev.*, 2015, **115**, 6217–6263.

11 Sousa, Sérgio Filipe and Ribeiro, António J M and Neves, Rui P P and Brás, Natércia F and Cerqueira, Nuno M F S A and Fernandes, Pedro A and Ramos, Maria João, *Wiley Interdiscip. Rev.: Comput. Mol. Sci.*, 2016, **7**, e1281–29.

12 Jógvan Magnus Haugaard Olsen and Jacob Kongsted, *Advances in Quantum Chemistry*, Elsevier, 2011, pp. 107–143.

13 Morzan, Uriel N and de Armiño, Diego J Alonso and Foglia, Nicolás O and Lebrero, Mariano C González and Scherlis, Damián A and Estrin, Darío A, *Chem. Rev.*, 2018, **118**, 4071–4113.

14 Mennucci, Benedetta and Corni, Stefano, *Nat. Rev. Chem.*, 2019, **2**, 1.

15 Thompson, Mark A and Schenter, Gregory K, *J. Phys. Chem.*, 1995, **99**, 6374–6386.

16 J. Gao, *Acc. Chem. Res.*, 1996, **29**, 298–305.

17 Van Duijnen, P T and Swart, M, *J. Phys. Chem. A*, 1998, **102**, 2399–2407.

18 Gordon, Mark S and Slipchenko, Lyudmilla and Li, Hui and Jensen, Jan H, *Annual Reports in Computational Chemistry*, Elsevier, 2007, pp. 177–193.

19 C. Curutchet, A. Muñoz-Losa, S. Monti, J. Kongsted, G. D.

Scholes and B. Mennucci, *J. Chem. Theory Comput.*, 2009, **5**, 1838–1848.

20 J. M. Olsen, K. Aidas and J. Kongsted, *J. Chem. Theory Comput.*, 2010, **6**, 3721–3734.

21 DeFusco, Albert and Minezawa, Noriyuki and Slipchenko, Lyudmila V. and Zahariev, Federico and Gordon, Mark S., *J. Phys. Chem. Lett.*, 2011, **2**, 2184–2192.

22 Gordon, Mark S. and Fedorov, Dmitri G. and Pruitt, Spencer R. and Slipchenko, Lyudmila V., *Chem. Rev.*, 2012, **112**, 632–672.

23 Gao, Jiali and Truhlar, Donald G and Wang, Yingjie and Mazack, Michael J M and Löffler, Patrick and Provorse, Makenzie R and Rehak, Pavel, *Acc. Chem. Res.*, 2014, **47**, 2837–2845.

24 D. Loco, L. Lagardère, S. Caprasecca, F. Lipparini, B. Mennucci and J.-P. Piquemal, *J. Chem. Theory Comput.*, 2017, **13**, 4025–4033.

25 Wu, Xiaojing and Teuler, Jean-Marie and Cailliez, Fabien and Clavaguéra, Carine and Salahub, Dennis R and de la Lande, Aurélien, *J. Chem. Theory Comput.*, 2017, **13**, 3985–4002.

26 D. Loco, L. Lagardère, G. A. Cisneros, G. Scalmani, M. Frisch, F. Lipparini, B. Mennucci and J.-P. Piquemal, *Chem. Sci.*, 2019, **10**, 7200–7211.

27 Valerio Vitale and Jacek Dziedzic and Alex Albaugh and Anders M. N. Niklasson and Teresa Head-Gordon and Chris-Kriton Skylaris, *J. Chem. Phys.*, 2017, **146**, 124115.

28 J. W. Ponder, C. Wu, P. Ren, V. S. Pande, J. D. Chodera, M. J. Schnieders, I. Haque, D. L. Mobley, D. S. Lambrecht, R. A. DiStasio, M. Head-Gordon, G. N. I. Clark, M. E. Johnson and T. Head-Gordon, *J. Phys. Chem. B*, 2010, **114**, 2549–2564.

29 J. Dziedzic, Y. Mao, Y. Shao, J. Ponder, T. Head-Gordon, M. Head-Gordon and C.-K. Skylaris, *J. Chem. Phys.*, 2016, **145**, 124106.

30 J. Dziedzic, T. Head-Gordon, M. Head-Gordon and C.-K. Skylaris, *J. Chem. Phys.*, 2019, **150**, 074103.

31 D. Loco, É. Polack, S. Caprasecca, L. Lagardère, F. Lipparini, J.-P. Piquemal and B. Mennucci, *J. Chem. Theory Comput.*, 2016, **12**, 3654–3661.

32 S. Caprasecca, S. Jurinovich, L. Lagardère, B. Stamm and F. Lipparini, *J. Chem. Theory Comput.*, 2015, **11**, 694–704.

33 F. Lipparini, *J. Chem. Theory Comput.*, 2019, **15**, 4312–4317.

34 J. A. Rackers, Z. Wang, C. Lu, M. L. Laury, L. Lagardère, M. J. Schnieders, J.-P. Piquemal, P. Ren and J. W. Ponder, *J. Chem. Theory Comput.*, 2018, **14**, 5273–5289.

35 L. Lagardère, L.-H. Jolly, F. Lipparini, F. Aviat, B. Stamm, Z. F. Jing, M. Harger, H. Torabifard, G. A. Cisneros, M. J. Schnieders, N. Gresh, Y. Maday, P. Y. Ren, J. W. Ponder and J.-P. Piquemal, *Chem. Sci.*, 2018, **99**, 956–972.

36 M. J. Frisch, G. W. Trucks, H. B. Schlegel, G. E. Scuseria, M. A. Robb, J. R. Cheeseman, G. Scalmani, V. Barone, G. A. Petersson, H. Nakatsuji, X. Li, M. Caricato, A. V. Marenich, J. Bloino, B. G. Janesko, R. Gomperts, B. Mennucci, H. P. Hratchian, J. V. Ortiz, A. F. Izmaylov, J. L. Sonnenberg, D. Williams-Young, F. Ding, F. Lipparini, F. Egidi, J. Goings, B. Peng, A. Petrone, T. Henderson, D. Ranasinghe, V. G. Zakrzewski, J. Gao, N. Rega, G. Zheng, W. Liang, M. Hada, M. Ehara, K. Toyota, R. Fukuda, J. Hasegawa, M. Ishida, T. Nakajima, Y. Honda, O. Kitao, H. Nakai, T. Vreven, K. Throssell, J. A. Montgomery, Jr., J. E. Peralta, F. Ogliaro, M. J. Bearpark, J. J. Heyd, E. N. Brothers, K. N. Kudin, V. N. Staroverov, T. A. Keith, R. Kobayashi, J. Normand, K. Raghavachari, A. P. Rendell, J. C. Burant, S. S. Iyengar, J. Tomasi, M. Cossi, J. M. Millam, M. Klene, C. Adamo, R. Cammi, J. W. Ochterski, R. L. Martin, K. Morokuma, O. Farkas, J. B. Foresman and D. J. Fox, *Gaussian 16 Revision A.03*, 2016.

37 M. F. S. J. Menger, S. Caprasecca and B. Mennucci, *J. Chem. Theory Comput.*, 2017, **13**, 3778–3786.

38 F. Lipparini, L. Lagardère, C. Raynaud, B. Stamm, E. Cancès, B. Mennucci, M. Schnieders, P. Ren, Y. Maday and J.-P. Piquemal, *J. Chem. Theory Comput.*, 2015, **11**, 623–634.

39 F. Lipparini, L. Lagardère, B. Stamm, E. Cancès, M. Schnieders, P. Ren, Y. Maday and J.-P. Piquemal, *J. Chem. Theory Comput.*, 2014, **10**, 1638–1651.

40 C. Jamorski, M. E. Casida and D. R. Salahub, *J. Chem. Phys.*, 1996, **104**, 5134–5147.

41 Ernest R. Davidson, *J. Comput. Phys.*, 1975, **17**, 87–94.

42 Cammi, R. and Tomasi, J., *Int. J. Quantum Chem.*, 1995, **56**, 465–474.

43 F. Furche and R. Ahlrichs, *J. Chem. Phys.*, 2002, **117**, 7433–7447.

44 G. Scalmani, M. J. Frisch, B. Mennucci, J. Tomasi, R. Cammi and V. Barone, *J. Chem. Phys.*, 2006, **124**, 094107.

45 I. Carnimeo, C. Cappelli and V. Barone, *J. Comput. Chem.*, 2015, **36**, 2271–2290.

46 N. C. Handy and H. F. Schaefer, *J. Chem. Phys.*, 1984, **81**, 5031–5033.

47 M. Frisch, M. Head-Gordon and J. Pople, *Chem. Phys.*, 1990, **141**, 189–196.

48 Wang,Wei and Skeel,Robert D. , *J. Chem. Phys.*, 2005, **123**, 164107.

49 L. Greengard and V. Rokhlin, *J. Comput. Phys.*, 1987, **73**, 325–348.

50 Eric G. Kratz and Alice R. Walker and Louis Lagardère and Filippo Lipparini and Jean-Philip Piquemal and G. Andrés Cisneros, *J. Comput. Chem.*, 2016, **37**, 1019–1029.

51 Sudholt, Wibke and Sobolewski, Andrzej L and Domcke, Wolfgang, *Chem. Phys.*, 1999, **240**, 9–18.

52 J. Dreyer and A. Kummrow, *J. Am. Chem. Soc.*, 2000, **122**, 2577–2585.

53 W. Fuß, K. K. Pushpa, W. Rettig, W. E. Schmid and S. A. Trushin, *Photochem. Photobiol. Sci.*, 2002, **1**, 255–262.

54 A. Köhn and C. Hättig, *J. Am. Chem. Soc.*, 2004, **126**, 7399–7410.

55 S. I. Druzhinin, N. P. Ernsting, S. A. Kovalenko, L. P. Lustres, T. A. Senyushkina and K. A. Zachariasse, *J. Phys. Chem. A*, 2006, **110**, 2955–2969.

56 Zachariasse, Klaas A and Druzhinin, Sergey I and Kovalenko, Sergey A and Senyushkina, Tamara, *J. Chem. Phys.*, 2009,

131, 224313–11.

57 T. Gustavsson, P. B. Coto, L. Serrano-Andrés, T. Fujiwara and E. C. Lim, *J. Chem. Phys.*, 2009, **131**, 031101.

58 P. B. Coto, L. Serrano-Andrés, T. Gustavsson, T. Fujiwara and E. C. Lim, *Phys. Chem. Chem. Phys.*, 2011, **13**, 15182.

59 M. Park, C. H. Kim and T. Joo, *J. Phys. Chem. A,* 2013, **117**, 370–377.

60 M. A. Kochman, A. Tajti, C. A. Morrison and R. J. D. Miller, *J. Chem. Theory Comput.*, 2015, **11**, 1118–1128.

61 B. F. E. Curchod, A. Sisto and T. J. Martínez, *J. Phys. Chem. A*, 2017, **121**, 265–276.

62 Michał Andrzej Kochman and Bo Durbeej, *J. Phys. Chem. A*, 2020, **124**, 2193–2206.

63 D. A. Case, I. Y. Ben-Shalom, S. R. Brozell, D. S. Cerutti, T. E. Cheatham, III, V. W. D. Cruzeiro, T. A. Darden, R. E. Duke, D. Ghoreishi, M. K. Gilson, H. Gohlke, A. W. Goetz, D. Greene, R. Harris, N. Homeyer, S. Izadi, A. Kovalenko, T. Kurtzman, T. S. Lee, S. LeGrand, P. Li, C. Lin, J. Liu, T. Luchko, R. Luo, D. J. Mermelstein, K. M. Merz, Y. Miao, G. Monard, C. Nguyen, H. Nguyen, I. Omelyan, A. Onufriev, F. Pan, R. Qi, D. R. Roe, A. Roitberg, C. Sagui, S. Schott-Verdugo, J. Shen, C. L. Simmerling, J. Smith, R. Salomon-Ferrer, J. Swails, R. C. Walker, J. Wang, H. Wei, R. M. Wolf, X. Wu, L. Xiao, D. M. York and P. A. Kollman, *AMBER 2018*, 2018.

64 J. Wang, R. M. Wolf, J. W. Caldwell, P. A. Kollman and D. A. Case, *J. Comput. Chem.*, 2004, **25**, 1157–1174.

65 H. J. C. Berendsen, J. P. M. Postma, W. F. van Gunsteren, A. DiNola and J. R. Haak, *J. Chem. Phys.*, 1984, **81**, 3684–3690.

66 J. Åqvist, P. Wennerström, M. Nervall, S. Bjelic and B. O. Brandsdal, *Chem. Phys. Lett.*, 2004, **384**, 288–294.

67 Jean-Paul Ryckaert and Giovanni Ciccotti and Herman J.C Berendsen, *J. Chem. Phys.*, 1977, **23**, 327–341.

68 Tom Darden and Darrin York and Lee Pedersen, *J. Chem. Phys*, 1993, **98**, 10089–10092.

69 Pengyu Ren and Jay W. Ponder, *J. Comput. Chem.*, 2002, **23**, 1497–1506.

70 Jay W. Ponder and David A. Case, *Protein Simulations*, Elsevier, 2003, pp. 27–85.

71 Pengyu Ren and Chuanjie Wu and Jay W. Ponder, *J. Chem. Theory Comput.*, 2011, **7**, 3143–3161.

72 Jonathan W. Essex and William L. Jorgensen, *J. Comput. Chem.*, 1995, **16**, 951–972.

73 N. Rega, G. Brancato and V. Barone, *Chem. Phys. Lett.*, 2006, **422**, 367–371.

74 H. Nguyen, D. R. Roe, J. Swails and D. A. Case, *Pytraj V1.0.0.Dev1: Interactive Data Analysis For Molecular Dynamics Simulations*, 2016.

75 D. R. Roe and T. E. Cheatham, *J. Chem. Theory Comput.*, 2013, **9**, 3084–3095.